


RESEARCH ARTICLE

WILEY

Biogeochemistry of low- and high-centered ice-wedge polygons in wetlands in Svalbard

Eleanor L. Jones^{1,2}  | Andrew J. Hodson^{1,3} | Kelly R. Redeker⁴ |
Hanne H. Christiansen⁵ | Steve F. Thornton⁶ | Jade Rogers⁶

¹Department of Arctic Geology, The University Centre in Svalbard, Longyearbyen, Norway

²Department of Geography, The University of Sheffield, Sheffield, UK

³Department of Environmental Sciences, Western Norway University of Applied Sciences, Sogndal, Norway

⁴Department of Biology, University of York, York, UK

⁵Department of Arctic Geophysics, The University Centre in Svalbard, Longyearbyen, Norway

⁶Department of Civil and Structural Engineering, The University of Sheffield, Sheffield, UK

Correspondence

Eleanor L. Jones, Department of Arctic Geology, The University Centre in Svalbard, Longyearbyen, Norway.
Email: eleanor.jones@sios-svalbard.org

Funding information

Joint Programming Initiative (JPI-Climate Topic 2: Russian Arctic and Boreal Systems), Grant/Award Number: 71126; NERC studentship, Grant/Award Number: NE/L002450; Research Council of Norway, Grant/Award Numbers: 294764, 20200053

Abstract

Arctic wetlands are a globally significant store of soil organic carbon. They are often characterized by ice-wedge polygons, which are diagnostic of lowland permafrost, and which greatly influence wetland hydrology and biogeochemistry during summer. The degradation of ice-wedge polygons, which can occur in response to climate change or local disturbance, has poorly understood consequences for biogeochemical processes. We therefore used geochemical analyses from the active layer and top permafrost to identify and compare the dominant biogeochemical processes in high-centered (degraded) and low-centered (pristine) polygons situated in the raised beach sediments and valley-infill sediments of Adventdalen, Central Svalbard. We found similar organic-rich sediments in both cases (up to 38 dry wt.%), but while low-centered polygons were water-saturated, their high-centered counterparts had a relatively dry active layer. Consequently, low-centered polygons showed evidence of iron and sulfate reduction leading to the precipitation of pyrite and siderite, whilst the high-centered polygons demonstrated more oxidizing conditions, with decreased iron oxidation and low preservation of iron and sulfate reduction products in the sediments. This study thus demonstrates the profound effect of ice-wedge polygon degradation on the redox chemistry of the host sediment and porewater, namely more oxidizing conditions, a decrease in iron reduction, and a decrease in the preservation of iron and sulfate reduction products.

KEYWORDS

biogeochemistry, ice-wedge polygon, permafrost, svalbard

1 | INTRODUCTION

Wetlands contain 20–30% of the 1,500 Pg of total soil carbon on Earth,¹ and low-relief wetlands cover a substantial area of the pan-Arctic landscape (<400,000 km²).² In the high Arctic, the formation of wetlands and peatlands in a polar desert depends on a reliable water

supply during the thaw season.^{3,4} The geomorphology of the landscape directly affects its hydrology¹ and the topographical setting of a wetland governs the inflows and outflows of water.⁴ In recently glaciated lowlands of the high Arctic, the topography is being modified by isostatic rebound, and periglacial and fluvial processes, all of which control the setting in which wetlands develop.⁴

This is an open access article under the terms of the [Creative Commons Attribution](https://creativecommons.org/licenses/by/4.0/) License, which permits use, distribution and reproduction in any medium, provided the original work is properly cited.

© 2023 The Authors. *Permafrost and Periglacial Processes* published by John Wiley & Sons Ltd.

At a smaller scale, ice-wedge polygons are widespread, ice-rich, and easily identifiable permafrost landforms,⁵ playing a role in the site-specific hydrology of wetlands (e.g., Liljedahl et al.⁶). Around 250,000 km² of the Arctic is covered by polygonal tundra.⁷ There are two main types of ice-wedge polygon: low-centered and high-centered.⁸ Low-centered polygons represent the first stage of ice-wedge development, while high-centered polygons occur only at a later stage.⁸ The change from low- to high-centered polygons can be caused by climate, local changes in geomorphology, or hydrological changes. The local topography developing from ice-wedge polygonal activity regulates the landscape hydrology.⁶ For example, the raised rims of low-centered polygons serve as hydrologic barriers, causing flooding of the centers of these polygons during summer.⁹

Ice-wedge polygons are vulnerable to climate change.¹⁰ In Alaska and several other Arctic sites, the degradation of ice wedges has increased as air temperatures have risen over the past 30 years.^{11–13} Differential ground subsidence occurs as the near-surface permafrost thaws and ice-wedges melt, causing polygons to become flat-centered and then eventually high-centered.⁹ The complete transformation of low-centered polygons to high-centered polygons has hydrologic implications, enabling the centers of high-centered polygons to drain via the connected troughs, causing drying of the landscape.^{12,14} However, in Svalbard, the ice-wedge morphology in Adventdalen has been stable for the last seven decades, despite a large increase in mean annual air temperature.¹⁵

Studies have shown that ice-wedge polygon morphology influences wetland biogeochemistry and hence organic carbon decomposition, with implications for greenhouse gas emissions from different polygon types.^{16–19} For example, the reduction of ferric iron in wetlands increases carbon dioxide production relative to methane production, and ferrihydrite minerals suppress methanogenesis by acting as energetically favorable electron acceptors, while crystalline iron oxides are not as easily reduced in anaerobic respiration and do not decrease methane production.^{20–22} However, few studies have investigated wetland biogeochemistry in areas with both low- and high-centered polygons by examining the variations with depth through the entire active layer and into the top permafrost. Although the spatial variability of carbon dioxide and methane fluxes has been described,^{15,23} and there is some previous work on the biogeochemistry of low-centered ice-wedge polygons,²⁴ there are no studies of high-centered polygons in Svalbard. The objective of this study is to characterize the dominant biogeochemical processes occurring in a high-centered polygon situated in a raised beach area in central Svalbard and compare this with low-centered polygons situated in a sediment-filled lowland valley area ~14 km further inland. In so doing, we use space-for-time substitution to provide insights into the potential for changing biogeochemical processes within the active layer in an area of continuous permafrost where permafrost degradation may eventually commence in coastal lowlands.¹⁵

2 | METHODOLOGY

2.1 | Field site description

Adventdalen (78°19'N, 15°93'E) is a valley, oriented NW–SE, and measuring 12 × 4 km, in central Svalbard. The lithology includes sedimentary rocks (sandstones, shales and carbonates) of the van Mijenfjord and Adventdalen Groups.²⁵ Svalbard's climate is polar tundra.²⁶ At Svalbard Airport, which is close to Adventdalen, the linear trend of mean annual air temperature from 1899 to 2018 indicates an increase of 3.7°C during this period, which includes a warming of 1.7°C per decade since 1991.²⁷ In the lower Adventdalen area, mean annual ground temperature (MAGT) at the depth of zero annual amplitude ranges from –5.2 to –2.5°C,²⁸ and a recent increase in permafrost temperature has been linked to the rising air temperature.²⁹ Permafrost thawed during the Last Glacial Maximum, when Adventdalen was filled with a dynamic and erosive ice stream.^{30–32} The subsequent glacial isostatic rebound of Svalbard meant that relative sea level fell, and a Gilbert-type delta prograded into Adventfjorden.^{33,34} In the valley bottom, permafrost between 0 and ~3 m depth formed syngenetically, as it aggraded concurrently with eolian sedimentation, whereas beneath this the permafrost aggraded epigenetically (following deposition of sediments, by downward freezing).³³ Here, the permafrost is now continuous, reaching a thickness of 80–100 m near the coast.^{31,35} In lower Adventdalen, the active layer thickness is between 60 and 205 cm, although this varies according to snow depth, amount of vegetation, and sediment type.^{28,36} This study is focussed on core-sampled material, down to 2 m depth, inclusive of the active layer and the top permafrost.

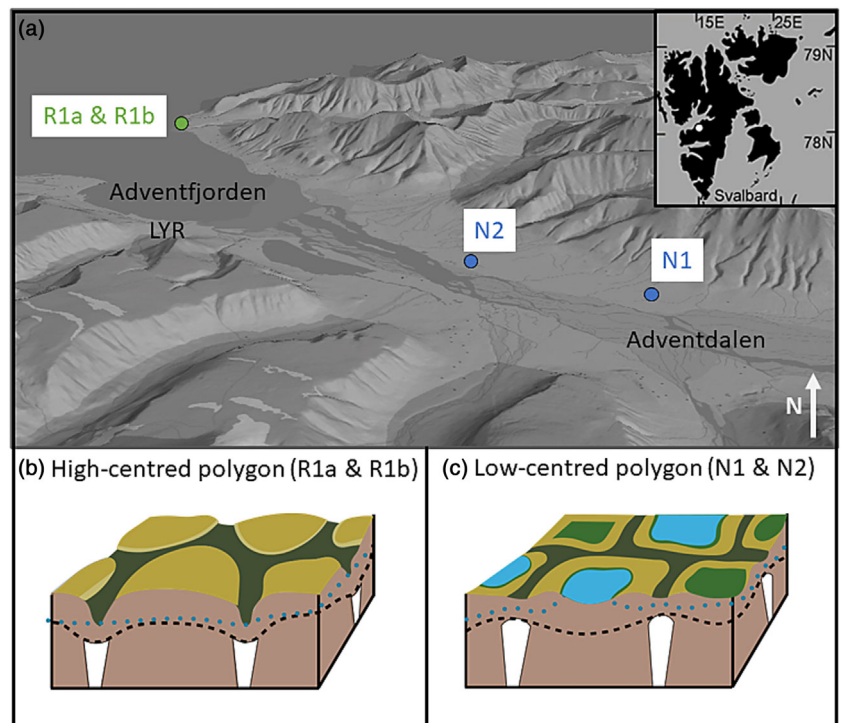
Table 1 lists the sample locations with details of the sampling area and Figure 1 shows the sampling locations and a schematic of the polygon structure. The low-centered polygons situated at Adventdalen North are covered with Late Holocene loess (eolian) deposits overlying alluvial and deltaic deposits.^{33,37} Adventdalen North is a water-saturated wetland, mainly fed by springs. The areas of the individual ice-wedge polygons studied at Adventdalen North were 90 m² (N2) and 270 m² (N1). The high-centered polygon studied is situated in peat deposits between raised beaches at Revneset. The area of this ice-wedge polygon was 99 m² (R1). The Adventdalen valley sediments are much thicker and more fine-grained than those at Revneset. The primary water source to Revneset is summer precipitation, with a probable contribution of meltwater from a late-lying snow bank (visible in Figure 2b). The mean pH of active layer water was 6.0 at Adventdalen North (ranging from 4.7 to 6.5), while the mean pH of active layer water was 5.7 at Revneset (ranging from 5.3 to 5.9).

The high-centered polygons at Revneset are evident from the aerial photographs in Figure 2b (1990) and Figure 2c (2009). While significant warming has occurred, especially on the coast,²⁷ local drainage changes might also have influenced the polygon development at Revneset.

TABLE 1 Site and sampling locations (coordinates in decimal degrees). Cores R1a and R1b are two different cores extracted from the center of the same ice-wedge polygon (R1).

Site	Site code	Latitude	Longitude	Elevation (m a.s.l.)	Sampling date
Adventdalen North	N1	78.20	15.99	10–15	02.05.16
	N2	78.21	15.87	5–10	15.04.14
Revneset	R1a	78.29	15.57	5–10	30.04.16
	R1b	78.29	15.57	5–10	26.04.16

FIGURE 1 (a) Map of the study site locations, with inset showing the study location on the Svalbard archipelago (map courtesy of the Norwegian Polar Institute), (b) schematic of high-centered ice-wedge polygons, representative of polygon R1, and (c) schematic of low-centered ice-wedge polygons, representative of polygons N1 and N2 (modified after Liljedahl et al.¹²). In (b) and (c), the blue dotted line represents the water table, whereas the black dashed line indicates the active layer depth. [Colour figure can be viewed at wileyonlinelibrary.com]



2.2 | Coring and core subdivision

A detailed methodology for the coring, core subdivision, pore water extractions, and chemical analyses is available in Jones et al.²⁴ Briefly, coring was undertaken in the polygon centers using hand drilling (a Stihl BT 130 drilling engine with a cylindrical drill head and rods) to a depth of 2 m in late winter before the onset of thaw, core segments were extruded into sterile Whirl Pak[®] bags, and transport and subdivision were conducted while maintaining frozen conditions. Cores were subdivided by sawing into 2-cm-depth slices while frozen. The freshly cut surfaces were scraped with a scalpel, and the outer 2 cm was removed with a hollow brass tube (3 cm in diameter), to prevent contamination. The sawblade, scalpel, and brass tube were cleaned with 70% isopropanol between slices.

In addition, in late summer 2017, thaw depths were measured three times in each polygon center using an active layer probe. The water table was measured once in late summer 2017 in the polygon centre.

2.3 | Pore water extractions

A pore water extraction method was adapted from Spence et al.³⁸ Vials containing samples were transferred to a Coy Vinyl Anaerobic chamber with an N₂ atmosphere (0 ppm oxygen). Each vial was weighed to determine the sample mass. Nitrogen-sparged de-ionized water (Milli-Q) was added to fill each vial. The vials were reweighed to determine the mass and volume of water added. A 3-mL volume of water was subsequently removed from the top of the vial to create a headspace. The vials were crimp-capped, inverted and stored for 5 days at 4°C whilst submerged in water (to prevent gas diffusion across the septa). This storage time enabled the de-ionized water to equilibrate with the sediment pore water (e.g., Spence et al.³⁸). Seven days after first saturation of the sample, the vials were centrifuged at 7,750 rpm for 5 min and transferred back to the anaerobic chamber. The equilibrated supernatant was filtered (0.22- μ m nylon syringe filter) for chemical analysis and the sediment remaining in the vials was weighed after drying at 105°C for

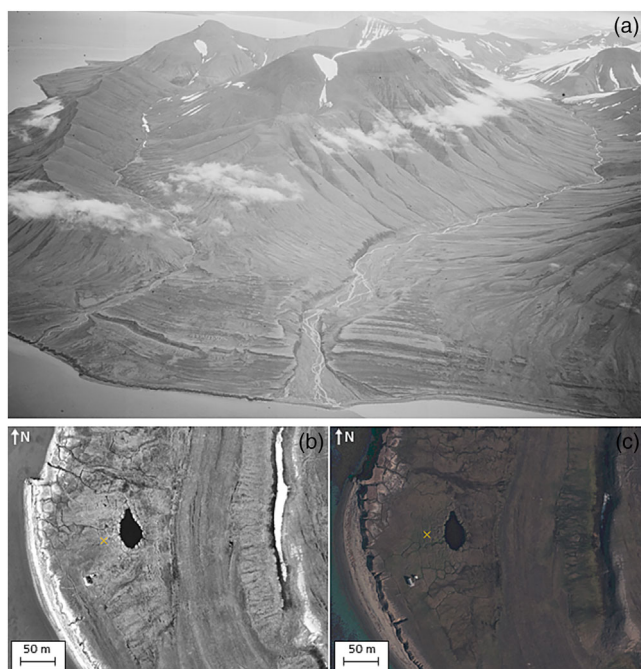


FIGURE 2 Time series of images of Revneset, showing (a) an overview of the site from 1936, facing northeast, (b) the site in summer 1990, and (c) the site in summer 2009. The orange cross marks R1. These historical photographs were provided by the Norwegian Polar Institute (reference numbers S36-3950, S90-1015, and S2009-13835-00132). [Colour figure can be viewed at wileyonlinelibrary.com]

24 h.^{39,40} The vials were then reweighed to determine the initial moisture content of the samples.

Cl^- and SO_4^{2-} in the extracted water were determined by ion chromatography (Dionex ion chromatograph, DX 90; limit of detection or “LOD” = 0.02 mg L^{-1} for the lowest, undiluted analysis; precision <5% for the mid-range standards). Trace metals (Fe, Mn) were determined on a 5-mL sample acidified with 50 μL of reagent-grade 69% HNO_3 (Fisher Scientific Trace Metal Grade), using inductively coupled plasma mass spectrometry (ICPMS; PerkinElmer Elan DRC II, MA, USA). The precision errors for repeat analyses of mid-range standards were <5%, and the detection limits were $1.0 \mu\text{g L}^{-1}$. Analyte concentrations were corrected for blank analyses and corrected for the dilution during the pore water extraction.

2.4 | Solid phase analyses

Carbon elemental abundance was determined by drying sediment samples at 105°C , acidifying in 6 M HCl, rinsing, drying, pulverising the <2-mm fraction in a Retsch ball mill for 5 min at 15.0 s^{-1} frequency, and analysing on an Elementar vario EL cube. Elemental concentrations were checked with acetanilide standards ($\text{C}_8\text{H}_9\text{NO}$; Merck; $n = 28$, % C = 70.96 ± 0.67 , % N = 10.34 ± 0.10), with two blanks and two acetanilide standards run every 15 samples.

The following solid phase analyses were conducted on cores N1 and R1a only. Acid-volatile sulfur (AVS) and chromium-reducible sulfur (CRS) were determined via a two-step distillation method applied to freeze-dried and milled sediment samples, first using 6 M HCl and then using boiling 3 M CrCl_2 solution.^{41,42} In each extraction, H_2S was precipitated as Ag_2S , filtered and dried, and sulfide was determined gravimetrically. The stoichiometry of the phase was used to convert the mass to weight per cent (FeS for AVS; FeS_2 for CRS).

Different operationally defined iron mineral phases were targeted with a four-step sequential extraction procedure applied to 100 mg of freeze-dried and milled sediment from one core at each site, following procedures from Raiswell et al.,⁴³ from Poulton and Canfield,⁴⁴ and detailed in Jones et al.²⁴ The phases extracted were (a) amorphous and nanoparticulate iron (oxyhydr)oxide phases ($\text{Fe}_{\text{ascorbate}}$), (b) iron bound in carbonates ($\text{Fe}_{\text{acetate}}$), (c) crystalline iron (oxyhydr)oxides ($\text{Fe}_{\text{dithionite}}$), and (d) magnetite ($\text{Fe}_{\text{oxalate}}$). These are linked to iron mineral phases based on standard assumptions about the mineralogy of the extracted phases (e.g., $\text{Fe}_{\text{dithionite}}$ is primarily crystalline iron [oxyhydr]oxides, $\text{Fe}_{\text{oxalate}}$ is primarily magnetite).

2.5 | Spatial analyses

The approximate proportion of high- and low-centered polygons between the raised beaches was estimated by visually classifying the polygons along the Revneset coastline, using high-resolution aerial imagery (where 1 mm on the photo represents 1,000 mm in reality) from 2009 from the Norwegian Polar Institute. A total of 139 polygons at Revneset and 1,212 polygons at Adventdalen North were classified by eye from these aerial images.

2.6 | Data analyses

Data analyses were performed in R⁴⁵ and graphics were prepared with the ggplot2 R package. Prior to testing correlations between variables, Shapiro-Wilk’s method was used to test whether data were normally distributed. Many variables were not normally distributed and their relationships with one another were nonlinear. This necessitated the use of the Spearman correlation test to examine monotonous relationships between the variables because it is robust to skewed distributions and outliers.⁴⁶

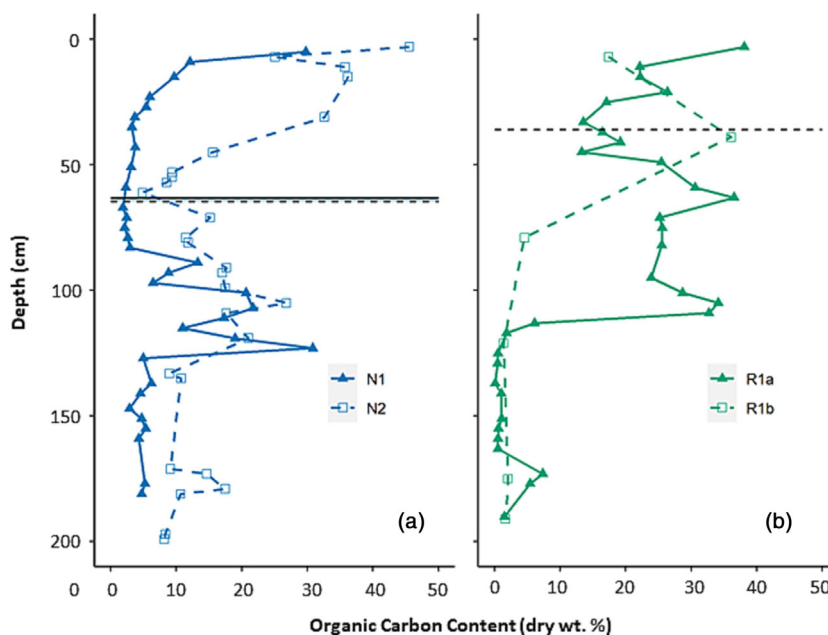
3 | RESULTS

Thaw depths in the low-centered N1 and N2 polygons were similar in late summer (63 and 65 cm, respectively; Table 2), while the thaw depth in the high-centered R1 polygon was shallower (36 cm; Table 2). Concurrently, the water table depth was shallow at both N1 and N2 (3 and 0 cm below the ground surface, respectively; Table 2), while the water table depth at R1a and R1b was much lower (31 cm below the ground surface; Table 2). At Revneset, 66% of a total of

TABLE 2 Thaw and water table depths in the polygon centers during late summer at Adventdalen North (N1 and N2) and Revneset (R1a and R1b), and summary statistics for the organic carbon content in all cores. Thaw depths are presented as a mean of three measurements within each polygon center, with the minimum and maximum thaw depth of each polygon in parentheses, and water table is one measurement, from the polygon center. Organic carbon content is presented as a mean of *n* measurements, with the minimum and maximum organic carbon content in parentheses.

Site	Date	Thaw depth (cm)	Water table depth below ground surface (cm)	Organic carbon content (dry wt.%, mean (min-max)) <i>n</i>
N1	31.08.17	63.3 (60.0–65.0)	3	8.55 (1.84–30.8) <i>n</i> = 33
N2	02.09.17	64.7 (62.0–68.0)	0	16.7 (4.83–45.6) <i>n</i> = 29
R1a	05.09.17	36.0 (34.0–39.0)	31	14.6 (0.09–38.1) <i>n</i> = 27
R1b	05.09.17	36.0 (34.0–39.0)	31	10.5 (1.38–36.1) <i>n</i> = 6

FIGURE 3 Organic carbon content with depth in cores (a) N1 and N2, and (b) R1a and R1b. The horizontal dashed line in (a) shows the thaw depth in N2 at the end of summer 2017, whereas the solid horizontal line shows the thaw depth in N1 at the end of summer 2017. The horizontal dashed line in (b) shows the thaw depth in R1 at the end of summer 2017. [Colour figure can be viewed at wileyonlinelibrary.com]



139 classified polygons were high-centered polygons, while 34% were low-centered polygons. In contrast, low-centered polygons were prevalent in Adventdalen,⁴⁷ and up-valley at the Adventdalen North site, 71% of a total of 1,212 classified polygons were low-centered.

All the cores from Adventdalen North and Revneset contained high organic carbon content at specific depths (Figure 3). N2 had the highest organic carbon content at the surface (45 dry wt.%; Figure 3a), a minimum in organic carbon content at 61 cm depth (5 dry wt.%), and a further peak in organic carbon content between 61 and 132 cm depth. N1 had slightly lower organic carbon content (Figure 3a), but trends with depth were similar to N2, in that the surface had the maximum organic carbon content (30 dry wt.%), which decreased with depth to 67 cm depth (1.84 dry wt.%), and rose again between 83 and 147 cm depth. R1a had a high organic carbon

content at the surface (38 dry wt.%; Figure 3b), which decreased to a minimum at 45 cm depth (13 dry wt.%), increased to a maximum between 45 and 109 cm depth, and reduced to very low content (~0.5 dry wt.%) below 109 cm depth. The profile from R1b was at a lower depth resolution, but clearly indicated a higher organic carbon content in the active layer and top permafrost, compared to the lower permafrost (Figure 3b).

Table 3 shows that the dominant iron phase at Revneset was $\text{Fe}_{\text{ascorbate}}$ (primarily ferrihydrite), whereas there were lower amounts of CRS (primarily pyrite) and $\text{Fe}_{\text{acetate}}$ (primarily siderite) at this site. In contrast, the sediments at Adventdalen North contained more CRS and $\text{Fe}_{\text{acetate}}$, but less $\text{Fe}_{\text{ascorbate}}$ (Table 3). Revneset contained more $\text{Fe}_{\text{dithionite}}$ (primarily crystalline iron [oxyhydr]oxides) than Adventdalen North (Table 3), and the amounts of $\text{Fe}_{\text{oxalate}}$ (primarily magnetite)

at both sites were variable, with the Adventdalen North sediments containing slightly more overall. Concentrations of AVS were low at both sites (Table 3).

TABLE 3 Summary statistics for the solid phase data from Revneset and Adventdalen North including AVS, CRS, $\text{Fe}_{\text{ascorbate}}$, $\text{Fe}_{\text{dithionite}}$, $\text{Fe}_{\text{acetate}}$, and $\text{Fe}_{\text{oxalate}}$.

Parameter	Dry wt.%	N1	R1a
AVS	Mean	0.02	0.007
	(min-max)	(0.00-0.05)	(0.00-0.04)
	n	7	8
CRS	Mean	0.12	0.077
	(min-max)	(0.02-0.27)	(0.017-0.16)
	n	7	8
$\text{Fe}_{\text{ascorbate}}$	Mean	0.97	1.04
	(min-max)	(0.32-1.64)	(0.18-3.26)
	n	10	8
$\text{Fe}_{\text{dithionite}}$	Mean	0.13	0.31
	(min-max)	(0.05-0.32)	(0.05-1.19)
	n	10	8
$\text{Fe}_{\text{acetate}}$	Mean	1.00	0.42
	(min-max)	(0.38-1.57)	(0.16-0.81)
	n	10	8
$\text{Fe}_{\text{oxalate}}$	Mean	1.58	0.52
	(min-max)	(0.55-3.43)	(0.05-2.10)
	n	10	8

The concentration of $\text{Fe}_{\text{(aq)}}$ in cores R1a and R1b was low ($<0.7 \text{ mmol L}^{-1}$; Figure 4b). In R1a, the concentration of $\text{Fe}_{\text{(aq)}}$ was lowest below 117 cm, whereas in R1b, the concentration was lowest below 75 cm. The concentrations of $\text{Fe}_{\text{(aq)}}$ were in general higher at Adventdalen North, with $\text{Fe}_{\text{(aq)}}$ in N1 reaching over 1.5 mmol L^{-1} ($\sim 150 \text{ cm}$ depth; Figure 4a). N2 had the highest concentrations, reaching 3 mmol L^{-1} at the base of the core (Figure 4a).

Concentrations of $\text{Mn}_{\text{(aq)}}$ were $<0.15 \text{ mmol L}^{-1}$ in all cores (Figure 5). Notable characteristics of the concentration profiles are that N1 displayed a peak in $\text{Mn}_{\text{(aq)}}$ at the active layer base (Figure 5a), N2 displayed a peak in $\text{Mn}_{\text{(aq)}}$ close to the ground surface (Figure 5a), and R1b displayed a peak in $\text{Mn}_{\text{(aq)}}$ close to the ground surface (Figure 5b).

Sulfate (SO_4^{2-}) concentrations in N1 were generally $<2 \text{ mmol L}^{-1}$, but they peaked at $>4 \text{ mmol L}^{-1}$ at the base of the active layer (Figure 6a). Sulfate (SO_4^{2-}) concentrations in N2 were the most consistently low of the four cores compared; they only rose above 1 mmol L^{-1} in one sample (Figure 6a). Sulfate (SO_4^{2-}) concentrations in R1a were $<0.30 \text{ mmol L}^{-1}$ down to 105 cm depth, below which they increased, rising to over 6 mmol L^{-1} at the core base (Figure 6b). Sulfate (SO_4^{2-}) concentrations in R1b were similarly low in the shallow sediments, but increased below 75 cm (Figure 6b).

Table 4 shows significant negative correlations between organic carbon and sulfate (SO_4^{2-}), as well as organic carbon and $\text{Mn}_{\text{(aq)}}$, while there are significant positive correlations between sulfate (SO_4^{2-}) and $\text{Mn}_{\text{(aq)}}$.

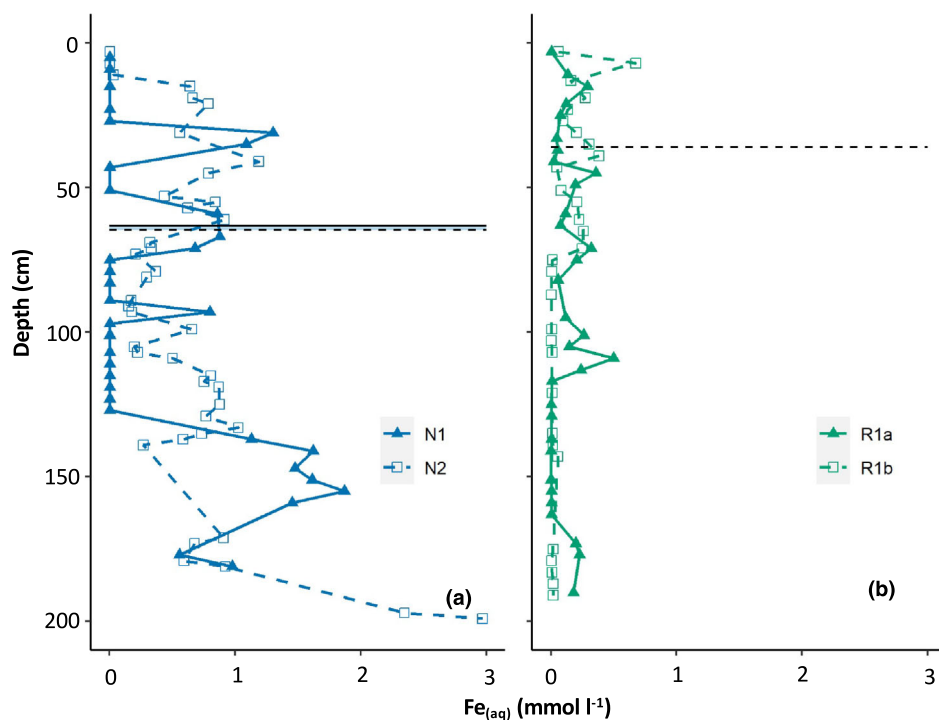


FIGURE 4 Aqueous iron ($\text{Fe}_{\text{(aq)}}$) with depth in cores (a) N1 and N2, and (b) R1a and R1b. The horizontal dashed line in (a) shows the thaw depth in N2 at the end of summer 2017, whereas the solid horizontal line shows the thaw depth in N1 at the end of summer 2017. The horizontal dashed line in (b) shows the thaw depth in R1 at the end of summer 2017. [Colour figure can be viewed at [wileyonlinelibrary.com](https://onlinelibrary.wiley.com/terms-and-conditions)] [wileyonlinelibrary.com](https://onlinelibrary.wiley.com/terms-and-conditions)]

FIGURE 5 Aqueous manganese ($Mn_{(aq)}$) with depth in cores (a) N1 and N2, and (b) R1a and R1b. The horizontal dashed line in (a) shows the thaw depth in N2 at the end of summer 2017, whereas the solid horizontal line shows the thaw depth in N1 at the end of summer 2017. The horizontal dashed line in (b) shows the thaw depth in R1 at the end of summer 2017. [Colour figure can be viewed at wileyonlinelibrary.com]

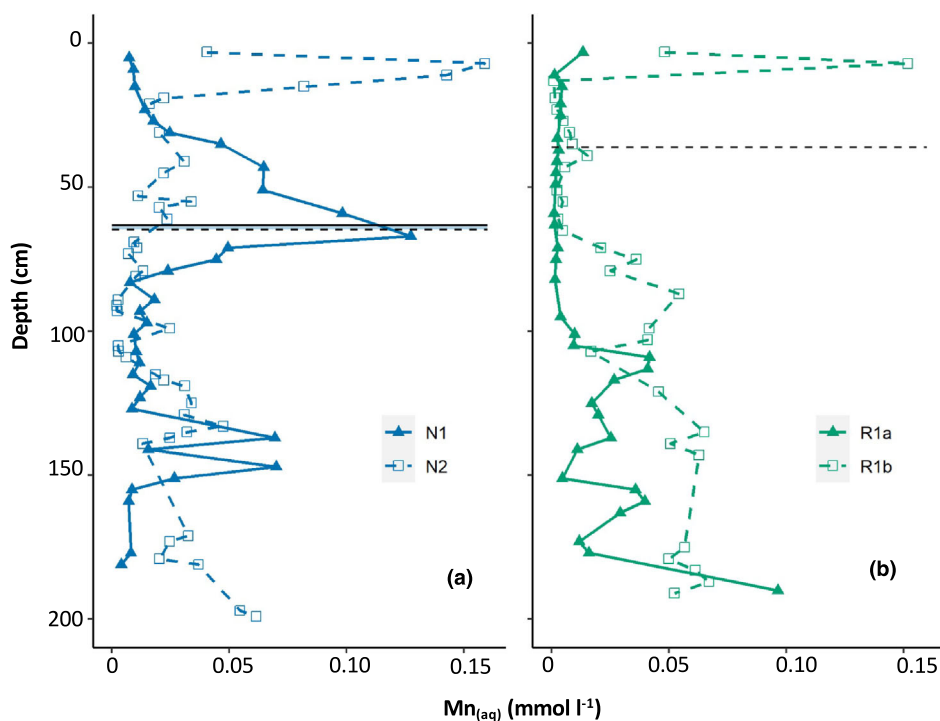


FIGURE 6 Sulfate (SO_4^{2-}) with depth in cores (a) N1 and N2, and (b) R1a and R1b. The horizontal dashed line in (a) shows the thaw depth in N2 at the end of summer 2017, whereas the solid horizontal line shows the thaw depth in N1 at the end of summer 2017. The horizontal dashed line in (b) shows the thaw depth in R1 at the end of summer 2017. [Colour figure can be viewed at wileyonlinelibrary.com]

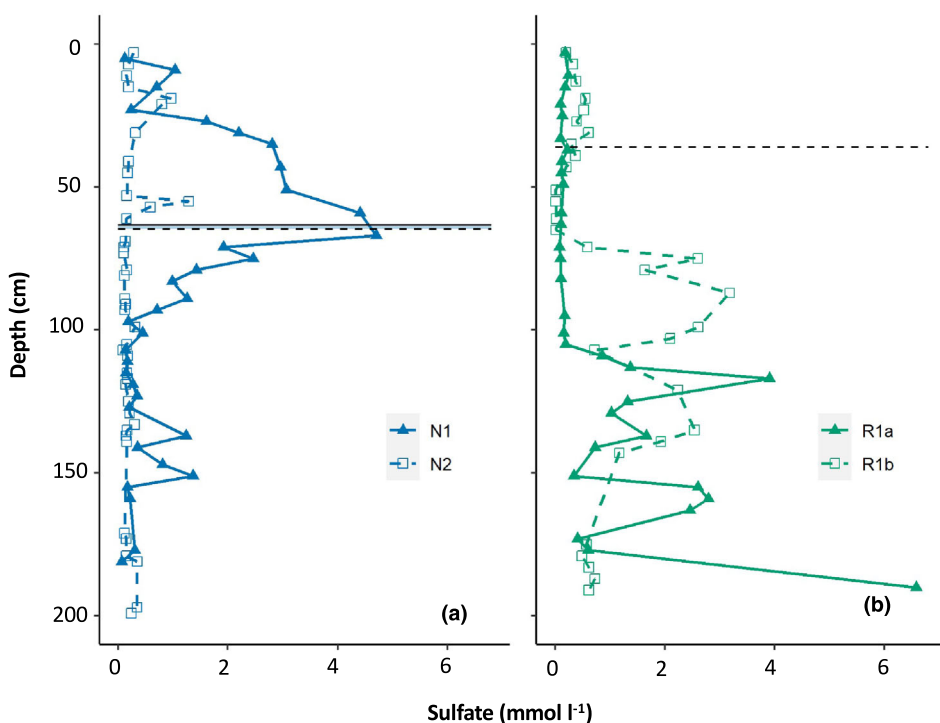


TABLE 4 Results of Spearman correlation testing between organic carbon, sulfate (SO_4^{2-}), and $Mn_{(aq)}$. Numbers represent correlation coefficients, while asterisks indicate the level of significance: ** $p < 0.01$, *** $p < 0.001$.

Parameter	All cores	N1	R1a
Organic carbon, SO_4^{2-}	-0.66***	-0.65***	-0.70***
Organic carbon, $Mn_{(aq)}$	-0.37***	-0.51**	-0.57**
SO_4^{2-} , $Mn_{(aq)}$	0.61***	0.80**	0.87***

4 | DISCUSSION

4.1 | Organic carbon accumulation

Cores from both Revneset and Adventdalen North contain an abundance of organic carbon sequestered in distinct depths of the active layer and permafrost (Figure 3). This high organic carbon content is characteristic of peat formed under anaerobic conditions, as net primary production generally exceeds decomposition under waterlogged conditions.⁴⁸ In ice-wedge polygonal tundra, anaerobic conditions are more likely in the centers of low-centered polygons because their rims impede water drainage, whereas the troughs of high-centered polygons facilitate relatively fast drainage of water from the polygonal networks (Figure 1).⁶ A high organic carbon content in the cores hence implies sediment deposition under anaerobic conditions in the center of low-centered polygons. This is consistent with the low-centered ice-wedge polygon morphology at Adventdalen North. However, the sampled polygon at Revneset was high-centered, with a high organic carbon content in the well-drained active layer. The high organic carbon content in the active layer and top permafrost suggests that (consistent with the theory developed by Mackay⁸) the polygon at Revneset has been transformed from low-centered and water-saturated to high-centered and well-drained.

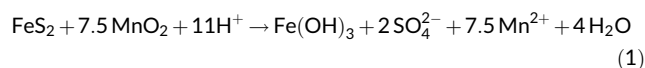
4.2 | Biogeochemical processes driving carbon dioxide production

Lipson et al.²² showed that the reduction of ferric iron increased carbon dioxide production while suppressing methane production and resulted in siderite formation in an Arctic peat soil in Alaska. The large amount of siderite relative to ferrihydrite at Adventdalen North is indicative of iron reduction, which suggests production of bicarbonate, leading to a high carbon dioxide emission potential (Table 3). Jones⁴⁹ reported up to 6462 $\mu\text{mol L}^{-1}$ carbon dioxide (as carbon dioxide, excluding bicarbonate) in active layer pore water of core N1 from Adventdalen North. In contrast, less iron reduction is evidenced at Revneset. Relatively low concentrations of siderite and pyrite are found at Revneset (Table 3); instead ferrihydrite, which is an amorphous, poorly crystalline iron oxide mineral that is precipitated as a result of the oxidation of Fe(II),⁵⁰ is the dominant solid iron phase close to the surface at Revneset. While the low and variable concentrations of Fe_(aq) in the active layer and top permafrost of Revneset (Figure 4) indicate that minor iron reduction occurs, the dominance of ferrihydrite indicates that iron oxidation exceeds iron reduction in the shallow sediments of Revneset.

The peak in Mn_(aq) concentrations near the ground surface in R1b and N2 is indicative of dissimilatory manganese reduction. This is common with marine sediments where there is often a depth sequence of electron acceptors used in sedimentary organic carbon oxidation, with Mn_(aq) peaking below oxygen and nitrate, but above Fe_(aq) and sulfate (SO₄²⁻) under steady-state conditions.⁵¹ Overall, however, we expect that dissimilatory manganese reduction is of

minor importance and a negligible contribution to carbon oxidation in these sediments. The pore water profiles provide stronger evidence that the oxidation of pyrite by manganese oxides was the mechanism which produced the observed Mn_(aq) concentrations (e.g., Schippers and Jorgensen⁵²). This mechanism of manganese reduction does not produce carbon dioxide because it is not directly linked to the oxidation of organic carbon. N1 shows a significant negative correlation between Mn_(aq) and organic carbon content ($\rho = -0.51$, $p < 0.01$; Table 4), as does R1 ($\rho = -0.57$, $p < 0.01$; Table 4), whereas we would expect the opposite if manganese reduction were linked to organic carbon oxidation. This indicates a probable role for the oxidation of pyrite by manganese oxides contributing Mn_(aq) to the pore water. The positive and highly significant correlation between Mn_(aq) and sulfate (SO₄²⁻) across all cores ($\rho = 0.61$, $p < 0.001$; Table 4) supports a coupling between manganese reduction and sulfide oxidation which provided Mn_(aq) across the landscape.

The oxidation of pyrite by manganese oxides in anoxic sediments was shown by Schippers and Jorgensen⁵² to proceed by the following equation:



The concentration of Mn_(aq) is substantially lower than that of sulfate (SO₄²⁻) in the cores and indicates that other mechanisms generate the surplus of sulfate (SO₄²⁻). Unlike in Adventdalen, where pyrite oxidation exerts a landscape-scale control over the concentrations of Fe_(aq) and sulfate,^{24,53} in the sites we compare here, iron and sulfate (SO₄²⁻) reduction mask the signatures of pyrite oxidation. Despite this, many samples from Adventdalen North and Revneset have a sulfate to chloride ratio greater than that of the snowpack (0.11: data not shown), suggesting that sulfide oxidation has enhanced sulfate (SO₄²⁻) concentrations. This proposed mechanism is supported by the absence of gypsum from the bedrock.⁵⁴ In addition, the release of sulfur from organic matter via microbial processing (e.g., Bartlett et al.⁵⁵) may contribute to the high sulfate to chloride ratio observed in these samples.

Consistent with anaerobic conditions, sulfate reduction occurred at both Revneset and Adventdalen North. Sulfate reduction is observed in permafrost settings less often than iron reduction, but Rivkina et al.⁵⁶ attributed acid-soluble sulfide in permafrost sediment samples from northeastern Siberia to an in-situ mechanism, indicative of sulfate reduction. Jones et al.²⁴ showed that in the absence of processes removing sulfate, the oxidative weathering of pyrite causes high concentrations of sulfate (SO₄²⁻) in Adventdalen permafrost (up to 20 mmol L⁻¹). As the catchment bedrock geology is the same for all our sites, we might expect to observe similarly high concentrations of sulfate (SO₄²⁻) in the porewaters to evolve if processes removing sulfate are not effective. The relatively low concentrations of sulfate (SO₄²⁻ <7 and <5 mmol L⁻¹ at Revneset and Adventdalen North respectively; Figure 6) therefore probably indicate sulfate reduction. In addition, there is a strong negative correlation between sulfate (SO₄²⁻) concentration and organic carbon content for all cores

($\rho = -0.66$, $p < 0.0001$), demonstrating a probable organic carbon control upon sulfate reduction. The control of organic carbon content on sulfate reduction has also been found in salt marsh sediments.⁵⁷

4.3 | Summary and predictions of the impact of permafrost thaw

In Adventdalen, organic carbon content and the degree of water saturation exert an important control on the prevailing biogeochemical processes, as has been observed in saturated active layer sediments (this study and Jones et al.²⁴). The sediments of the low-centered polygons of Adventdalen North are water-saturated, rich in organic carbon, and anaerobic, with iron and sulfate reduction leading to the precipitation of pyrite and siderite. High rates of these microbial processes are fostered by eolian deposition of reactive, fine mineral dusts. In contrast, the active layer of the high-centered polygon at Revneset is not susceptible to eolian deposition of fine sediments and has a lower water table due to degradation of the ice wedges allowing drainage. This has led to more oxidizing conditions in the high-centered polygon, despite the high organic carbon content of the active layer, with a dominance of iron oxidation at Revneset; ferrihydrite is the dominant extracted iron phase and there are much lower levels of pyrite and siderite. The low water table precludes the formation and/or preservation of pyrite, even though sulfate reduction occurs in the active layer at Revneset. While the concentrations of $Mn_{(aq)}$ at both sites indicate the reduction of manganese oxides, this is not coupled to the oxidation of organic carbon, but rather to the oxidation of pyrite. Hence, dissimilatory manganese reduction does not produce substantial quantities of carbon dioxide at either site.

Permafrost in Svalbard is relatively warm for its northerly latitude,⁵⁸ and there has been a warming of 1.7°C per decade at Svalbard Airport since 1991.²⁷ Despite this, occurrences of extremely high summer temperatures have so far been limited by the maritime climate on Svalbard.¹⁵ This may explain the absence of ice-wedge degradation in Adventdalen, as extremely high summer temperatures have been a trigger of ice-wedge degradation in Alaska.^{11,12,15} In addition, the acceleration of wind channelized along the Adventdalen valley provides reduced snow thickness and efficient ground cooling in winter.⁵⁹ Matsuoka et al.⁶⁰ identified that present ice-wedge activity in Adventdalen is largely controlled by cold winter spells, thus enabling ongoing ice-wedge formation even during warming conditions. Pirk et al.¹⁵ suggest that as temperature increases markedly in Svalbard, this may cause future ice-wedge polygon degradation in Adventdalen. At Revneset, the previous polygon degradation resulted in drainage of the center of the polygon and an oxidation of the active layer. The impact of future ice-wedge degradation at Adventdalen North is likely to result in drainage, oxidation of pyrite and siderite, and increased aerobic respiration, with consequent increases in carbon dioxide fluxes to the atmosphere. Although the Adventdalen valley sediments are much thicker and more fine-grained than those at Revneset, and hence potentially more concerning for greenhouse gas emissions under future warming and permafrost thaw, the

particularly organic-rich sediments are mainly confined to the upper 2 m.³⁷ The data presented in this study demonstrate the profound effect of ice-wedge polygon drainage on the sediment and porewater biogeochemistry: polygon drainage results in more oxidizing conditions, a decrease in iron reduction, and a decrease in the preservation of the products of iron and sulfate reduction.

ACKNOWLEDGEMENTS

Gwilym Jones, Gunnar Mallon, Graham Gilbert, Ebbe Bak, Dotan Rotem, Yishai Weinstein, Sarah St Germain, Simon Norum, and Knut Lindland Tveit are thanked for their field assistance, and Alan Smalley, Rob Ashurst, Joe Hufton, Andy Fairburn, Roscoe Blevins, Anthony Turner, and Andy Hobson are thanked for their assistance with the laboratory analyses. Much of the content of this paper appears online in EJ's PhD thesis.⁴⁹

DATA AVAILABILITY STATEMENT

Jones.⁴⁹ Permafrost and active layer biogeochemical data from Adventdalen (2015–2017) (Version 1.0) in the UK Polar Data Centre, Natural Environment Research Council, UK Research & Innovation (<https://doi.org/10.5285/4c90d954-3db2-4084-9fe9-e050c839a6fe>).

ORCID

Eleanor L. Jones  <https://orcid.org/0000-0002-5556-7915>

REFERENCES

- Mitsch WJ, Gosselink JG. *Wetlands*. 5th ed. Wiley; 2007.
- Walker DA, Reynolds MK, Daniëls FJA, et al. The circumpolar Arctic vegetation map. *J Veg Sci*. 2005;16(3):267-282. doi:10.1111/j.1654-1103.2005.tb02365.x
- Martini IP, Glooschenko WA. Cold climate peat formation in Canada, and its relevance to lower Permian coal measures of Australia. *Earth Sci Rev*. 1985;22(2):107-140. doi:10.1016/0012-8252(85)90003-0
- Woo M, Young KL. High Arctic wetlands: their occurrence, hydrological characteristics and sustainability. *J Hydrol*. 2006;320(3-4):432-450. doi:10.1016/j.jhydrol.2005.07.025
- Christiansen HH, Matsuoka N, Watanabe T. Progress in understanding the dynamics, internal structure and Palaeoenvironmental potential of ice wedges and sand wedges. *Permafrost Periglacial Process*. 2016;27(4):365-376. doi:10.1002/ppp.1920
- Liljedahl AK, Hinzman LD, Schulla J. Ice-wedge polygon type controls low-gradient watershed-scale hydrology. Tenth International Conference on Permafrost; 2012:231-236.
- Minke M, Donner N, Karpov NS, De Klerk P, Joosten H. Distribution, diversity, development and dynamics of polygon mires: examples from NE Yakutia (NE Siberia). *Peatlands Int*. 2007;1:36-40.
- Mackay JR. Thermally induced movements in ice-wedge polygons, western Arctic coast: a long-term study. *Géograph Phys Quatern*. 2000;54(1):41-68. doi:10.7202/004846ar
- Liljedahl AK. The hydrological regime at sub-arctic and arctic watersheds: present and projected. *PhD Thesis*. University of Alaska, Fairbanks; 2011.
- Jorgenson MT, Kanevskiy M, Shur Y, et al. Role of ground ice dynamics and ecological feedbacks in recent ice wedge degradation and stabilization. *J Geophys Res Earth*. 2015;120(11):2280-2297. doi:10.1002/2015JF003602
- Jorgenson MT, Shur YL, Pullman ER. Abrupt increase in permafrost degradation in Arctic Alaska. *Geophys Res Lett*. 2006;33(2):L02503.

12. Liljedahl AK, Boike J, Daanen RP, et al. Pan-Arctic ice-wedge degradation in warming permafrost and influence on tundra hydrology. *Nat Geosci.* 2016;9(4):312-318. doi:10.1038/ngeo2674
13. Reynolds MK, Walker DA, Ambrosius KJ, et al. Cumulative geoeological effects of 62 years of infrastructure and climate change in ice-rich permafrost landscapes, Prudhoe Bay oilfield, Alaska. *Glob Chang Biol.* 2014;20(4):1211-1224. doi:10.1111/gcb.12500
14. Godin E, Fortier D, Lévesque E. Nonlinear thermal and moisture response of ice-wedge polygons to permafrost disturbance increases heterogeneity of high Arctic wetland. *Biogeosciences.* 2016;13(5):1439-1452. doi:10.5194/bg-13-1439-2016
15. Pirk N, Sievers J, Mertes J, Parmentier FJW, Mastepanov M, Christensen TR. Spatial variability of CO₂ uptake in polygonal tundra: assessing low-frequency disturbances in eddy covariance flux estimates. *Biogeosciences.* 2017;14(12):3157-3169. doi:10.5194/bg-14-3157-2017
16. Lara MJ, Mcguire AD, Euskirchen ES, et al. Polygonal tundra geomorphological change in response to warming alters future CO₂ and CH₄ flux on the Barrow peninsula. *Glob Chang Biol.* 2015;21(4):1634-1651. doi:10.1111/gcb.12757
17. Newman BD, Throckmorton HM, Graham DE, et al. Microtopographic and depth controls on active layer chemistry in Arctic polygonal ground. *Geophys Res Lett.* 2015;42(6):1808-1817. doi:10.1002/2014GL02804
18. Sachs T, Giebels M, Boike J, Kutzbach L. Environmental controls on CH₄ emission from polygonal tundra on the microsite scale in the Lena river delta, Siberia. *Glob Chang Biol.* 2010;16(11):3096-3110.
19. Wainwright HM, Dafflon B, Smith LJ, et al. Identifying multiscale zonation and assessing the relative importance of polygons geomorphology on carbon fluxes in an Arctic tundra ecosystem. *J Geophys Res Biogeo.* 2015;707-723.
20. Herndon EM, Yang Z, Bargar J, et al. Geochemical drivers of organic matter decomposition in arctic tundra soils. *Biogeochemistry.* 2015;126(3):397-414. doi:10.1007/s10533-015-0165-5
21. Herndon E, AlBashaireh A, Singer D, Roy Chowdhury T, Gu B, Graham D. Influence of iron redox cycling on organo-mineral associations in Arctic tundra soil. *Geochim Cosmochim Acta.* 2017;207:210-231. doi:10.1016/j.gca.2017.02.034
22. Lipson DA, Jha M, Raab TK, Oechel WC. Reduction of iron (III) and humic substances plays a major role in anaerobic respiration in an Arctic peat soil. *J Geophys Res Biogeo.* 2010;115(4):G00I06.
23. Pirk N, Mastepanov M, López-Blanco E, et al. Toward a statistical description of methane emissions from arctic wetlands. *Ambio.* 2017b;46(S1):70-80. doi:10.1007/s13280-016-0893-3
24. Jones EL, Hodson AJ, Thornton SF, et al. Biogeochemical processes in the active layer and permafrost of a high Arctic Fjord valley. *Front Earth Sci.* 2020;8:342. doi:10.3389/feart.2020.00342
25. Dallmann WK, Midbø PS, Nøttvedt A, Steel RJ. Lithostratigraphic lexicon of Svalbard: review and recommendations for nomenclature use: upper Palaeozoic to quaternary bedrock, Norsk Polarinstittutt, pp 318, 1999.
26. Kottke M, Grieser J, Beck C, Rudolf B, Rubel F. World map of the Köppen-Geiger climate classification updated. *Meteorol Z.* 2006;15(3):259-263. doi:10.1127/0941-2948/2006/0130
27. Nordli Ø, Wyszynski P, Gjeltén HM, et al. Revisiting the extended Svalbard airport monthly temperature series, and the compiled corresponding daily series 1898-2018. *Polar Res.* 2020;39:3614. doi:10.33265/polar.v39.3614
28. Christiansen HH, Gilbert GL, Neumann U, et al. Ground ice content, drilling methods and equipment and permafrost dynamics in Svalbard 2016-2016 (PermaSval). In: Moreno-Ibáñez M, Hagen JO, Hübner C, Lihavainen H, Zaborska A, eds. *SESS Report 2020, Svalbard Integrated Arctic Earth Observing System, Longyearbyen*; 2020:259-275. doi:10.5281/zenodo.4294095
29. Isaksen K, Sollid JL, Holmlund P, Harris C. Recent warming of mountain permafrost in Svalbard and Scandinavia. *J Geophys Res.* 2007;112(F2):F02S04.
30. Humlum O, Instanes A, Sollid JL. Permafrost in Svalbard: a review of research history, climatic background and engineering challenges. *Polar Res.* 2003;22(2):191-215. doi:10.3402/polar.v22i2.6455
31. Humlum O. Holocene permafrost aggradation in Svalbard. *Geol Soc Lond Spec Publ.* 2005;242(1):119-129. doi:10.1144/GSL.SP.2005.242.01.11
32. Landvik JY, Ingólfsson Ó, Mienert J, et al. Rethinking late Weichselian ice-sheet dynamics in coastal NW Svalbard. *Boreas.* 2005;34(1):7-24. doi:10.1080/03009480510012809
33. Gilbert GL, O'Neill HB, Nemeč W, Thiel C, Christiansen HH, Buylaert J-P. Late Quaternary sedimentation and permafrost development in a Svalbard fjord-valley, Norwegian high Arctic. *Sedimentology.* 2018;65(7):2531-2558.
34. Lønne I, Nemeč W. High-arctic fan delta recording deglaciation and environment disequilibrium. *Sedimentology.* 2004;51(3):553-589. doi:10.1111/j.1365-3091.2004.00636.x
35. Brown J, Ferrians OJ Jr, Heginbottom JA, Melnikov ES. Circum-Arctic map of permafrost and ground-ice conditions. *U.S. Geological Survey, Map CP-45*, US Department of the Interior. 1997.
36. Christiansen HH, Etmüller B, Isaksen K, et al. The thermal state of permafrost in the nordic area during the international polar year 2007-2009. *Permafrost Periglacial Process.* 2010;21(2):156-181. doi:10.1002/ppp.687
37. Cable S, Elberling B, Kroon A. Holocene permafrost history and cryostratigraphy in the high-Arctic Adventdalen Valley, Central Svalbard. *Boreas.* 2017;47(2):423-442.
38. Spence MJ, Thornton SF, Bottrell SH, Spence KH. Determination of interstitial water chemistry and porosity in consolidated aquifer materials by diffusion equilibrium-exchange. *Environ Sci Technol.* 2005;39(4):1158-1166. doi:10.1021/es049401v
39. Ernakovich JG, Lynch LM, Brewer PE, Calderon FJ, Wallenstein MD. Redox and temperature-sensitive changes in microbial communities and soil chemistry dictate greenhouse gas loss from thawed permafrost. *Biogeochemistry.* 2017;134(1-2):183-200. doi:10.1007/s10533-017-0354-5
40. Kokelj SV, Burn CR. Ground ice and soluble cations in near-surface permafrost, Inuvik, Northwest Territories, Canada. *Permafrost Periglacial Process.* 2003;14(3):275-289. doi:10.1002/ppp.458
41. Canfield DE, Raiswell R, Westrich JT, Reaves CM, Berner RA. The use of chromium reduction in the analysis of reduced inorganic sulfur in sediments and shales. *Chem Geol.* 1986;54(1-2):149-155. doi:10.1016/0009-2541(86)90078-1
42. Fossing H, Barker Jørgensen B. Measurement of bacterial sulfate reduction in sediments: evaluation of a single-step chromium reduction method. *Biogeochemistry.* 1989;8(3):205-222.
43. Raiswell R, Benning LG, Tranter M, Tulaczyk S. Bioavailable iron in the Southern Ocean: the significance of the iceberg conveyor belt. *Geochem Trans.* 2008;9:1-9.
44. Poulton SW, Canfield DE. Development of a sequential extraction procedure for iron: implications for iron partitioning in continentally derived particulates. *Chem Geol.* 2005;214(3-4):209-221. doi:10.1016/j.chemgeo.2004.09.003
45. R Core Team. R: a language and environment for statistical computing. 2021. R Foundation for Statistical Computing, Vienna, Austria. <https://www.R-project.org/>
46. du Prel J-B, Rohrig B, Hommel G, Blettner M. Choosing statistical tests: part 12 of a series on evaluation of scientific publications. *Dtsch Arztebl Int.* 2010;107(19):343-348. doi:10.3238/arztebl.2010.0343
47. Sørbel L, Tolgensbakk J. Ice-wedge polygons and solifluction in the Adventdalen area, Spitsbergen, Svalbard. *Nor Geogr Tidsskr - nor J Geogr.* 2002;56(2):62-66. doi:10.1080/00291950270056369

48. Kolka R, Bridgham S, Ping C-L. Soils of peatlands: Histosols and Gelisols. In: *Wetland Soils*. CRC Press; 2015:277-310.
49. Jones E. The Biogeochemistry of the Active Layer and Shallow Permafrost in a High Arctic Fjord Valley, Svalbard. Ph. D. thesis. University of Sheffield; 2019.
50. Megonigal JP, Hines ME. Anaerobic metabolism: linkages to trace gases and aerobic processes. *Treatise Geochem Biogeochem*. 2004;8:317-424.
51. Froelich PN, Klinkhammer GP, Bender ML, et al. Early oxidation of organic matter in pelagic sediments of the eastern equatorial Atlantic: suhoxic diagenesis. *Geochim Cosmochim Acta*. 1978;43:1075-1090.
52. Schippers A, Jorgensen BB. Oxidation of pyrite and iron sulfide by manganese dioxide in marine sediments. *Geochim Cosmochim Acta*. 2001;65(6):915-922. doi:10.1016/S0016-7037(00)00589-5
53. Hodson A, Nowak A, Christiansen H. Glacial and periglacial floodplain sediments regulate hydrologic transfer of reactive iron to a high arctic fjord. *Hydrol Process*. 2016;30(8):1219-1229. doi:10.1002/hyp.10701
54. Svinth AAG. A sedimentological and Petrographical investigation of the Todalen member and the boundary beds of the Endalen member: within the Firkanten formation (Paleocene) in the Central Basin of Spitsbergen, Svalbard. *Unpublished Masters Thesis*, Norwegian University; 2013.
55. Bartlett R, Bottrell SH, Coulson JP, Lee J, Forbes L. ³⁴S tracer study of pollutant sulfate behaviour in a lowland peatland. *Biogeochemistry*. 2009;95(2-3):261-275. doi:10.1007/s10533-009-9335-7
56. Rivkina E, Gilichinsky D, Wagener S, Tiedje J, McGrath J. Biogeochemical activity of anaerobic microorganisms from buried permafrost sediments. *Geomicrobiol J*. 1998;15(3):187-193. doi:10.1080/01490459809378075
57. Antler G, Mills JV, Hutchings AM, Redeker KR, Turchyn AV. The sedimentary carbon-sulfur-iron interplay—a lesson from east Anglian salt marsh sediments. *Front Earth Sci*. 2019;7:140. doi:10.3389/feart.2019.00140
58. Romanovsky VE, Smith SL, Christiansen HH. Permafrost thermal state in the polar northern hemisphere during the international polar year 2007–2009: a synthesis. *Permafrost Periglac Process*. 2010;21(2):106-116. doi:10.1002/ppp.689
59. Christiansen HH, Humlum O, Eckerstorfer M. Central Svalbard 2000–2011 meteorological dynamics and periglacial landscape response. *Arct Antarct Alp Res*. 2013;45(1):6-18. doi:10.1657/1938-4246-45.16
60. Matsuoka N, Christiansen HH, Watanabe T. Ice wedge seasonal deformation and thermal contraction cracking in Svalbard: lessons from a decade of automated monitoring. *Permafrost Periglac Process*. 2018;29(3):210-227. doi:10.1002/ppp.1985

How to cite this article: Jones EL, Hodson AJ, Redeker KR, Christiansen HH, Thornton SF, Rogers J. Biogeochemistry of low- and high-centered ice-wedge polygons in wetlands in Svalbard. *Permafrost and Periglac Process*. 2023;1-11. doi:10.1002/ppp.2192